



# Effect of Cold Rolling and Heat Treatment on Corrosion and Wear Behavior of $\beta$ -Titanium Ti-25Nb-25Zr Alloy

Prabhat K. Rai, D. Naidu, S.K. Vajpai, B. Sharma, K. Ameyama, and K. Mondal

Submitted: 9 January 2021 / Revised: 22 March 2021 / Accepted: 28 March 2021 / Published online: 16 April 2021

**This work discusses the effect of cold rolling and subsequent annealing on the corrosion and wear behavior of a  $\beta$ -type commercial Ti-25Nb-25Zr alloy. Using the cold-rolling and heat treatment, samples with different grain sizes were produced from the alloy. The effect of microstructural evolution due to cold rolling and annealing treatment on the corrosion behavior was examined in the Hank's simulated body fluid solutions, whereas sliding wear behavior was analyzed using ball-on-disk tribometer under dry condition. The corrosion resistance of the alloy was found to improve with cold rolling and subsequent annealing treatment. Increase in grain size also led to the improvement in the corrosion resistance in the Hank's simulated body fluid solution. Wear resistance was found to be highest for the sample annealed at 400 °C due to its highest hardness among all the samples. Abrasive wear was found to be the dominating wear mechanism.**

**Keywords** cold rolling, corrosion, Ti-25Nb-25Zr alloy, wear

## 1. Introduction

Owing to the outstanding properties, like low modulus of elasticity, high specific strength, good biocompatibility and excellent corrosion resistance,  $\alpha/\beta$ -type Ti-6Al-4V alloys are widely used Ti alloys for bio-implant materials (Ref 1-4). However, it has been reported that the release of Al and V ions from Ti-6Al-4V alloys causes various health issues, like osteomalacia, neuropathy and Alzheimer diseases (Ref 5, 6). In addition to this, these alloys have higher modulus of elasticity than bone tissues leading to bone resorption, implant loosening and failure when used as orthopaedic implant materials (Ref 7). Therefore, substitution of Al and V by other potential elements in Ti-based alloys has been attempted in the recent past. Song et al. (Ref 8) have shown that the modulus of elasticity of conventional Ti alloys can be decreased by alloying with elements, like Zr, Nb, Mo and Ta, without affecting the strength. Moreover, various alloys of Ti containing Nb, Zr, Ta, etc., have been studied in the past and found to be non-toxic (Ref 9).

In addition to the strength, modulus of elasticity and non-toxicity, properties like corrosion and wear resistance are also important because the implants undergo corrosive dissolution

and wear in the human body. The severe environment for implant materials inside the human body contains  $K^+$ ,  $Na^+$ ,  $Mg^{+2}$ ,  $Ca^{+2}$ , chloride, bicarbonate, phosphate, proteins, plasma and dissolved oxygen, etc. (Ref 10, 11). Therefore, in vitro study of implant materials to evaluate their corrosion performance is generally carried out in Hank's or Ringer's simulated body fluid solution (Ref 12). In addition to the composition of body fluid, shifting of equilibrium by biological molecules, like proteins, presence of bacteria, change in pH and change in oxygen concentration near implants, are also important factors, which control the release of metal ions from implant material (Ref 12). Therefore, effect of alloying elements on the corrosion behavior of various implant materials has been extensively studied (Ref 12). Jeong et al. (Ref 13) have studied the effect of Zr addition on corrosion behavior of Ti-35Nb-xZr alloys containing 3wt.% to 10 wt.% Zr in 0.9% NaCl solution. The Ti-35Nb-xZr alloy containing 10 wt.% Zr has exhibited highest corrosion resistance among all the studied alloys. It has been concluded that increase in Zr content causes the improvement in corrosion resistance. Geetha et al. (Ref 14) have studied the effect of heat treatment and resulting microstructural changes on the corrosion behavior of a Ti-13Nb-13Zr alloy in Ringer's solution. They have concluded that equiaxed microstructure and homogeneous distribution of alloying elements (Nb and Zr) are beneficial for the improvement in corrosion resistance. In contrast to this, depletion of Nb can result in the reduction in corrosion resistance.

The corrosion resistance of Ti-alloys primarily depends on the thickness, composition and kinetics of the formation of passive oxide film in physiological medium (Ref 15). Therefore, the possibility of failure of implants is increased due to the combined effect of wear and corrosion (tribo-corrosion) since wear results in damage of protective oxide film and crack initiation (Ref 16, 17). Moreover, the initial surface damage of the implants due to corrosion and wear also reduces their fatigue resistance. Sahoo et al. (Ref 18) have shown that wear behavior of Ti-alloys are affected by microstructural variation. Li et al. (Ref 19) have reported that the wear behavior of a Ti-29Nb-13Ta-4.6Zr alloy improves with an increase in Nb content and oxidizing treatment due to the formation of

**Prabhat K. Rai**, Research and Development, JSW Steel Ltd, Vijayanagar Works, Bellary, Karnataka 583275, India; **D. Naidu** and **K. Mondal**, Department of Materials Science and Engineering, Indian Institute of Technology Kanpur, Kanpur, UP 208016, India; **S.K. Vajpai**, Department of Materials and Metallurgical Engineering, National Institute of Technology, Jamshedpur, Jharkhand 831014, India; **B. Sharma**, Research Organization of Science and Technology, Ritsumeikan University, 1-1-1 Noji-Higashi, Kusatsu, Shiga 525-8577, Japan; and **K. Ameyama**, Faculty of Science and Engineering, Ritsumeikan University, Kusatsu, Shiga 5258577, Japan. Contact e-mail: prabhatrai2008@gmail.com.

lubricating Nb<sub>2</sub>O<sub>5</sub>. Corrosion and sliding wear behavior of a martensitic Ti-13Nb-13Zr alloy has been compared with a martensitic and a ( $\alpha + \beta$ ) Ti-6Al-4V ELI alloys (Ref 15). It has been found that the wear resistance of the Ti-13Nb-13Zr alloy is lower than that of the Ti-6Al-4V ELI alloys with both kind of microstructures due to the lowest hardness of the former. However, corrosion resistance of the Ti-13Nb-13Zr is lower than that of the martensitic Ti-6Al-4V ELI alloy and higher than that of the ( $\alpha + \beta$ ) Ti-6Al-4V ELI alloys in Ringer's solution.

Ralston et al. (Ref 20) have suggested that grain size and crystallographic texture affect the corrosion behavior to a large extent. Generally, grain refinement causes increase in the corrosion resistance in passive medium and vice-versa in active medium. Balyanov et al. (Ref 21) have studied the effect of grain size on the commercially pure Ti in HCl and H<sub>2</sub>SO<sub>4</sub> acids and found higher corrosion resistance of the ultra-fine grained (UFG) Ti as compared to its coarse grained counterpart due to better and rapid passivation of UFG Ti. Hoseini et al. (Ref 22) have studied the effect of grain size and crystallographic texture on the corrosion behavior of commercially pure Ti in 0.16 mol/L NaCl solution, and found that texture dominates the grain size in affecting the corrosion behavior. Therefore, it is clear from the above discussion that composition, processing and resulting microstructural changes play an important role in deciding the corrosion and wear resistance of Ti-based alloys.

Vajpai et al. (Ref 23) have studied the effect of cold rolling and subsequent annealing at different temperatures on the microstructure and corresponding mechanical properties of  $\beta$ -type Ti-25Nb-25Zr alloy. However, corrosion and wear behavior for this alloy has not been studied. Moreover, as indicated in the literature, grain size and their distribution affects the corrosion and wear behavior of the metals and alloys significantly (Ref 24, 25). Therefore, in the present work, effect of microstructural changes (grain size) induced by the cold-rolling and subsequent annealing at different temperatures on the corrosion behavior of  $\beta$ -type Ti-25Nb-25Zr alloy have been studied in Hank's simulated body fluid solution, whereas sliding wear behavior has been investigated using ball-on-disc tribometer under dry condition. The obtained results have been analyzed and involved mechanisms have been discussed.

## 2. Experimental

The initial samples of Ti-25Nb-25Zr (wt.%) alloy was received in the form of rods of  $\sim 5.97$  mm diameter in the solution-treated (ST) condition. The chemical composition of the initial samples is listed in Table 1. The multi-pass rolling of rods was carried out at room temperature to prepare strips with a  $\sim 1.29$  mm thickness. Reduction in thickness was  $\sim 80\%$ . Thereafter, the rolled samples were annealed at 400 °C, 600 °C, 800 °C, and 1000 °C, for 3600 s in an ultra-high vacuum furnace. For metallographic analysis, the samples were

ground with SiC papers followed by cloth polishing. Samples were etched with Kroll's reagent (HCl, HNO<sub>3</sub>, H<sub>2</sub>O in 2:1:3 ratio) solution. The microstructure of the initial, rolled and annealed samples were examined using Scanning Electron Microscopy (Jeol JSM-7200F).

Electrochemical tests were carried out using PARSTAT 2263 potentiostat. Flat bottom cell comprising of three electrodes were used for electrochemical tests. A saturated calomel electrode ( $E_{SCE}^0 = +241\text{mV}_{SCE}$ ) and a platinum mesh were used as reference electrode and counter electrode, respectively. The experiments were conducted in a freely aerated Hank's simulated body fluid solution which was prepared by mixing KCl (0.4 g/L), NaCl (8 g/L), NaHCO<sub>3</sub> (0.35 g/L), CaCl<sub>2</sub> (0.14 g/L), Na<sub>2</sub>HPO<sub>4</sub>·2H<sub>2</sub>O (0.06 g/L), MgSO<sub>4</sub>·7H<sub>2</sub>O (0.06 g/L), KH<sub>2</sub>PO<sub>4</sub> (0.6 g/L), MgCl<sub>2</sub>·6H<sub>2</sub>O (0.1 g/L) and glucose (1.0 g/L) (Ref 25). The pH of the electrolyte was maintained at 7.4. Samples were exposed to electrolyte for 3600 s for stabilization of the open circuit potential (OCP). Potentio-dynamic polarization experiments were conducted at a scan rate of 0.166 mV/s. The corrosion current density was determined using Tafel extrapolation method, and corrosion rate (mm/year) was calculated according to ASTM G-102 89 (Ref 26). Afterward, corroded samples were analyzed with the help of FEI-Nova Field Emission-Scanning Electron Microscope (FE-SEM).

Micro-hardness was measured with the help of Bareiss Prüfgerätebau GmbH hardness tester. Holding time and load during micro-hardness measurement were used as 10 seconds and 0.5N, respectively. Wear behavior of all the samples were analyzed using a tribometer (DUCOM TR-20LE-PHM500) in a ball-on-disk arrangement. The sample and a tungsten carbide (WC) ball of 10 mm diameter were used as a disc and counter body, respectively. The wear tests were carried out at a rotational speed of 200 rpm and normal load of 5N for one hour while maintaining the wear track diameter of 3.5 mm under dry-sliding conditions at room temperature.

## 3. Results and Discussion

The microstructure of the initial rod samples is shown in SEM images (Fig. 1). From Fig. 1(a), it is clear that the microstructure of as-received rod consists of two distinct regions: Area-I with equiaxed grains and Area-II with unresolved features. SEM image of the Area-I at high magnification (Fig. 1b) shows that the Area-I consists of equi-axed grains with size in the range of 3-5  $\mu\text{m}$  which could be due to complete recrystallization. On the other hand, SEM images of Area-II at high magnification shows the grains of sizes  $\leq 1 \mu\text{m}$  (fine-grained area) which could be due to partial recrystallization.

The microstructure of the cross-sectional surface of the cold-rolled samples is shown in Fig. 2. The microstructure exhibits the presence of severely deformed and elongated grains, along

**Table 1 Chemical composition of as-received Ti-25Nb-25Zr alloy**

Elements	Nb	Zr	Fe	C	N	H	O	Ti
Composition, wt.%	24.6	25.2	0.08	0.03	0.01	0.01	0.08	Balance

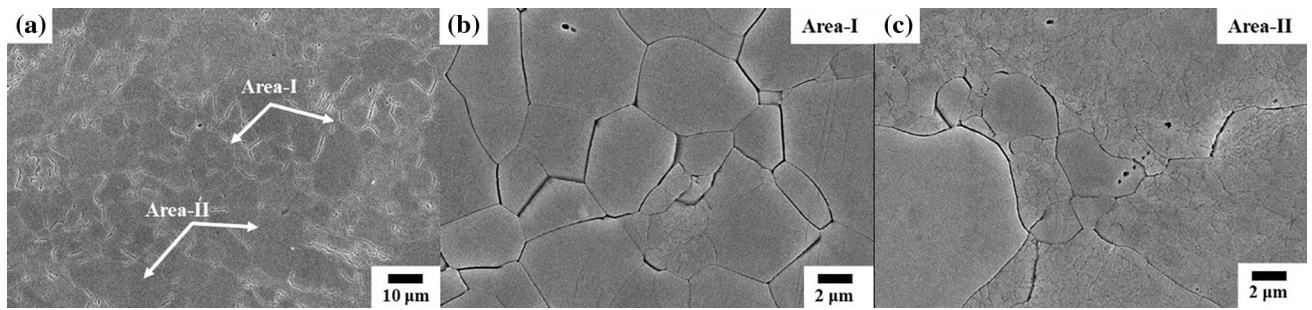


**Fig. 1** Representative SEM micrographs of (a) Ti-25Nb-25Zr initial rod and high magnification micrographs of (b) Area-I and (c) Area-II of (a)

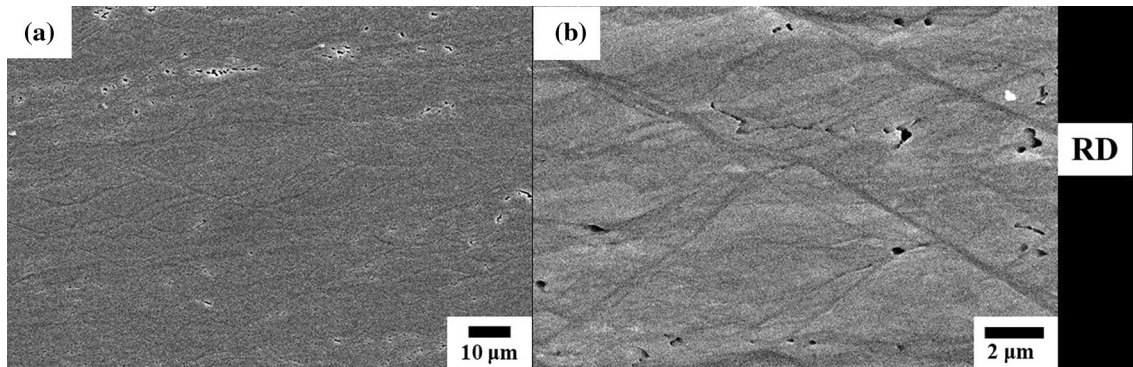


**Fig. 2** SEM micrographs of a cold-rolled strip of Ti-25Nb-25Zr alloy at (a) low and (b) high magnification

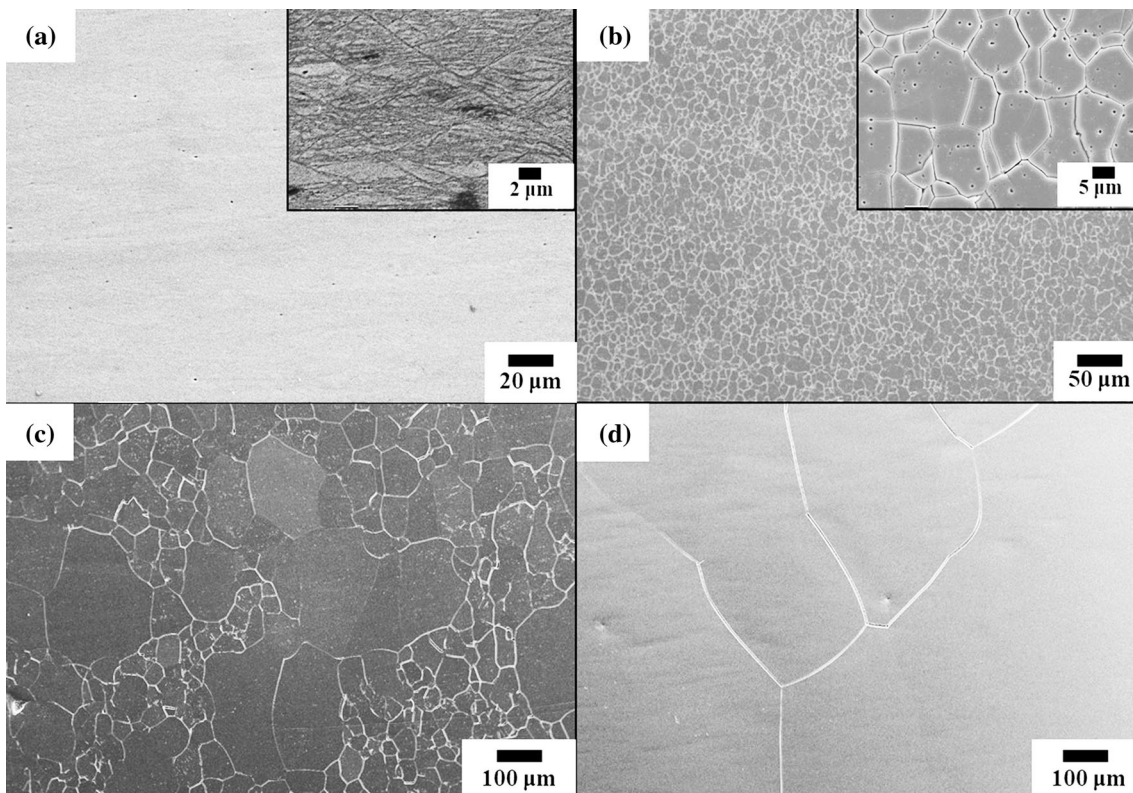


**Fig. 3** SEM micrographs of a cold-rolled strip of Ti-25Nb-25Zr alloy after annealing at (a) 400 °C, (b) 600 °C, (c) 800 °C and (d) 1000 °C. The high magnification images of (a) and (b) is shown in the inset.

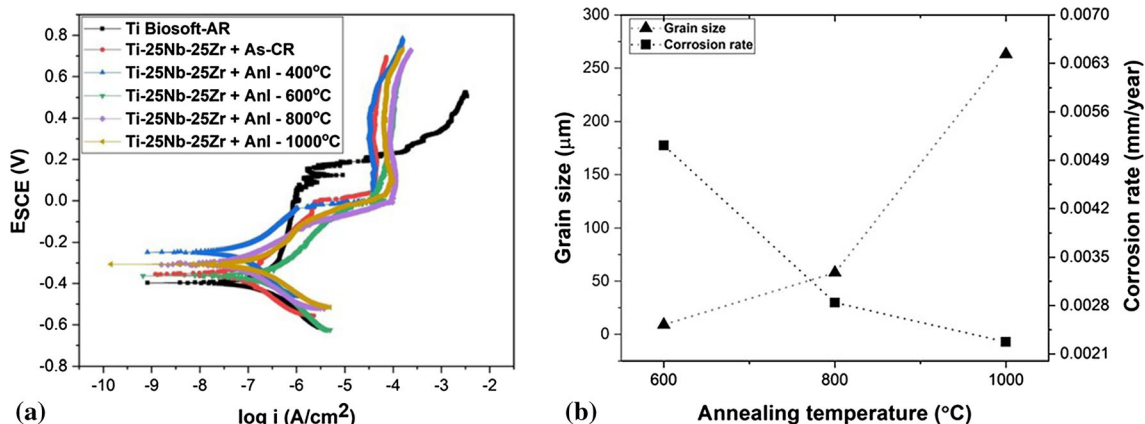
with shear bands. The SEM micrographs of the cold-rolled Ti-25Nb-25Zr alloy samples after annealing from 400 to 1000 °C are shown in Fig. 3(a-d). It can be noticed that the specimen annealed at a low temperature of 400 °C (Fig. 3a) exhibits deformed structure, as in the case of the cold-rolled specimen as shown in Fig. 2. Therefore, it can be concluded that the annealing at low temperatures could not cause any observable microstructural evolution except some amount of localized recovery/recrystallization, resulting in the formation of small-sized sub-grains. Therefore, it is clear that the annealing at 400 °C, results in stress-relieving along with a plausible recovery.

Figure 3(b) shows the SEM micrographs of the cold-rolled Ti-25Nb-25Zr samples after annealing at 600 °C. The recrystallized and equiaxed fine grains of grain size  $\sim 9 \mu\text{m}$  can be observed. Instead, it can be noticed that the annealing at 800 °C (Fig. 3c) and 1000 °C (Fig. 3d) have led to a significantly coarse-grained equiaxed microstructure with grain size,  $\sim 58 \mu\text{m}$  and  $\sim 263 \mu\text{m}$ , respectively. Vajpai et al. (Ref 23) have demonstrated with the help of XRD analysis that the  $\beta$ -type Ti-25Nb-25Zr alloys are stable against severe plastic deformation and no signature of strain induced phase transformation could be observed after cold rolling. However, they have found the precipitation of HCP  $\alpha$ -phase in the samples annealed at 400 °C, whereas single phase ( $\beta$ -phase) exists in the samples annealed at 600 °C, 800 °C and 1000 °C. It is plausible that the generation of large number of defects due to the cold rolling offers the heterogeneous nucleation sites for  $\alpha$ -phase (HCP) precipitation at low temperature annealing (400 °C). The  $\alpha$ -phase could not be observed even in high magnification SE/BSE images as well as EBSD analysis. It can be due to the small content of  $\alpha$ -phase whose presence could only be revealed by small peaks in XRD analysis as shown in Ref 23. It could be due to the presence of Nb which acts as a strong  $\beta$ -stabilizer. Zhang et al. (Ref 27) have reported that Nb ( $\beta$ -stabilizer) affects the  $\beta$ -transus temperature significantly, whereas Zr acts as neutral element and does not influence the  $\beta$ -transus temperature considerably. They have reported  $\beta$ -transus temperature of Ti-24Nb-2Zr alloy to be 833 K which could also be assumed for the present alloy.

Dynamic polarization tests were conducted to understand the electrochemical behavior of the samples in the wider potential range in Hank's simulated body fluid solution (Fig. 4a). The corrosion current density,  $i_{\text{CORR}}$  was estimated

using Tafel extrapolation method and the obtained values along with the values of  $\beta_a$  and  $\beta_c$  have been listed in Table 2.  $\beta_a$  and  $\beta_c$  are the slope of linear portion of anodic and cathodic branch of the polarization plot. It is clear from Table 3 that the corrosion current density of the cold rolled sample is lower than that of the as-received sample. The improvement in corrosion resistance after cold rolling can be attributed to the possible crystallographic texture induced in the sample due to the cold rolling. Guo et al. (Ref 28) have also reported the improvement in corrosion resistance of the Ti-6Al-3Nb-2Zr-1Mo alloy after cold rolling due to crystallographic texture. However, the corrosion resistance further improves after annealing the cold-rolled sample at 400 °C. It has already been mentioned that only recovery takes place after annealing at 400 °C, and no signature of recrystallization has been found. It is well known that the density of defects, like dislocations, vacancy, etc., and other microstructural heterogeneities get reduced after recovery resulting in lowering of energy. This could be the reason of slightly improved corrosion resistance of sample annealed at 400 °C as compared to the cold-rolled sample. However, recrystallization began to take place after annealing at temperatures higher than 600 °C resulting in formation and growth of new strain-free grains. It is worth to mention here that it would be unfair to compare the corrosion resistance of textured cold-rolled sample and sample annealed at 400 °C with fully recrystallized samples after annealing at 600 to 1000 °C. It is due to the fact that corrosion resistance of material is strongly influenced by grain size, defect density, crystallographic texture, surface energy, etc. (Ref 20). Hoseini et al. (Ref 22) have reported that crystallographic texture influences the corrosion resistance of commercially pure-Ti more than grain size does. Therefore, corrosion resistance of fully recrystallized samples annealed at 600 to 1000 °C has been compared with the as-received sample so that the effect of grain size and crystallographic texture can be studied.

The corrosion rates obtained from the samples annealed at temperatures 600, 800 and 1000 °C have been plotted against the corresponding grain sizes and presented in Fig. 4(b). The grain size of the as-received sample could not be included in the plot due to its bimodal grain size distribution. It is clear that the corrosion rate decreases with increase in the grain size (Fig. 4b). It can be noticed that the corrosion rate of the sample annealed at 600 °C is comparable with that of the as-received sample (Table 2). However, the corrosion rate



**Fig. 4** (a) Dynamic polarization plot obtained after potentiodynamic polarization test in Hank's simulated body fluid (b) variation of corrosion rate with grain size

**Table 2 Electrochemical parameters obtained from dynamic polarization test in Hank's simulated body fluid**

Samples	$\beta_a$ , mV/decade	$\beta_c$ , mV/decade	$E_{corr}$ , mV versus SCE	$i_{corr}$ , $\mu\text{A}/\text{cm}^2$	CR, mm/year
Ti-biosoft	338	171	-263	0.25	0.0047
Cold rolled	255	229	-354	0.12	0.0023
Annealed at 400 °C	235	235	-254	0.096	0.0018
Annealed at 600 °C	218	217	-374	0.27	0.0051
Annealed at 800 °C	191	218	-310	0.15	0.0028
Annealed at 1000 °C	203	197	-313	0.12	0.0023

**Table 3 Micro-hardness of as-received, cold-rolled and annealed Ti-25Nb-25Zr samples**

Samples	Micro-hardness (HV)
Ti-Biosoft	210 ± 13
Cold rolled	265 ± 10
Annealed at 400 °C	340 ± 11
Annealed at 600 °C	224 ± 9
Annealed at 800 °C	220 ± 15
Annealed at 1000 °C	215 ± 13

significantly reduces after annealing the samples at 800 and 1000 °C (Fig. 4b). Decrease in the corrosion rate or increase in the corrosion resistance can be attributed to the increase in grain size with annealing temperature. The effect of grain size on the corrosion rate is not significant in case of the as-received sample and the sample annealed at 600 °C due to the small difference (5 to 8  $\mu\text{m}$ ) in grain size of the two samples. However, significant grain growth occurs after annealing at higher temperatures, which can bring appreciable change in the corrosion rate. Due to the higher energy, grain boundaries are anodic to grain interior and more vulnerable sites for corrosive attack. As grain boundary density decreases with increase in grain size, the number of anodic sites decreases resulting in the enhancement of corrosion resistance.

In addition to the grain size, it has been found in our previous work (Ref 23) that the intensity of XRD peak corresponding to  $\beta(211)$  phase increases significantly with increase in the annealing temperature. It indicates that the tendency of preferred crystallographic texture increases with increase in the annealing temperature. Similar tendency has also been observed from EBSD analysis before (Ref 23). Therefore, it can be concluded that the combined effect of increase in grain size and crystallographic texture has attributed to improvement in the corrosion resistance with increase in the annealing temperature.

Difference in passivation behavior of the as-received sample and the annealed samples can be easily noticed in Fig. 4. The as-received sample has shown initial tendency of passivation, but could not continue beyond the potential of 170 mV with respect to standard calomel electrode (SCE). On the other hand, the stable passivation continues up to 650 mV versus SCE in case of the cold rolled and annealed samples. The difference in passivation could be attributed to recrystallized and partially recrystallized regions present in the as-received sample resulting in differential passivation kinetics. Serrations present just below the break down potential in the anodic branch of

dynamic polarization plot suggest the occurrence of unstable passivation kinetics. Similar to corrosion current density, passive current densities of the cold-rolled and sample annealed at 400 °C is lower than that of the samples annealed at higher temperature. Therefore, it can be concluded that the cold rolling followed by recovery improves the corrosion resistance and passivation kinetics.

The corroded surfaces of the samples after dynamic polarization test has been analyzed using scanning electron microscope and shown in Fig. 5(a-f). It is clear from the SEM micrographs of the samples after dynamic polarization test that the samples have not gone severe dissolution even after the anodic polarization of 1 Volt with respect to SCE. This is consistent with low current density (high corrosion resistance) of Ti-based alloys. Some pits have been observed in case of the as-received sample as shown in the inset of Fig. 5(a). This can be attributed to the early breakdown of the passive film as indicated by lower breakdown potential of as-received sample in Fig. 4. However, small pits can be observed in SEM micrograph of corroded surface of annealed samples as shown in the inset of Fig. 5(d) as a representative image of other samples. This could be due to the plausible initiation of pitting at higher potentials as indicated by increasing trend of current density at the end of anodic branch of polarization plots of cold rolled and annealed samples (Fig. 4). Effect of grain size can also be observed in the SEM images of the corroded surfaces of the annealed samples (Fig. 5d-f). Inset of Fig. 5(d) shows that pits formed in the sample annealed at 600 °C are finer as compared to those in the samples annealed at 800 °C (Fig. 5e) and 1000 °C (Fig. 5f) as shown by dotted circles. Moreover, number of pits is more in case of the sample annealed at 600 °C as compared to those in the samples annealed at 800 °C and 1000 °C. This could be attributed to the difference in grain size and resulting difference in grain boundary densities in the samples annealed at different temperatures. The mechanism is shown with the schematic (Fig. 6). Since the grain boundaries are anodic with respect to grain interior, the probability of pit formation at the grain boundaries and triple junctions is significantly higher than that in the grain interior leading to an increase in corrosion current density. But, the growth of pit is limited by the growth of adjacent pit initiated at another nearby grain boundaries resulting in finer pits as shown with the dotted circles in the schematic (Fig. 6). However, in case of the samples with coarser grain, the number of pits is less but bigger in size (Fig. 6d).

Table 3 presents the micro-hardness values of the as-received, the cold-rolled and the annealed samples. It is clear that the micro-hardness has increased after cold rolling from 210 ± 17 to 265 ± 11 HV, which can be attributed to the strain hardening caused by cold-deformation. Micro-hardness has

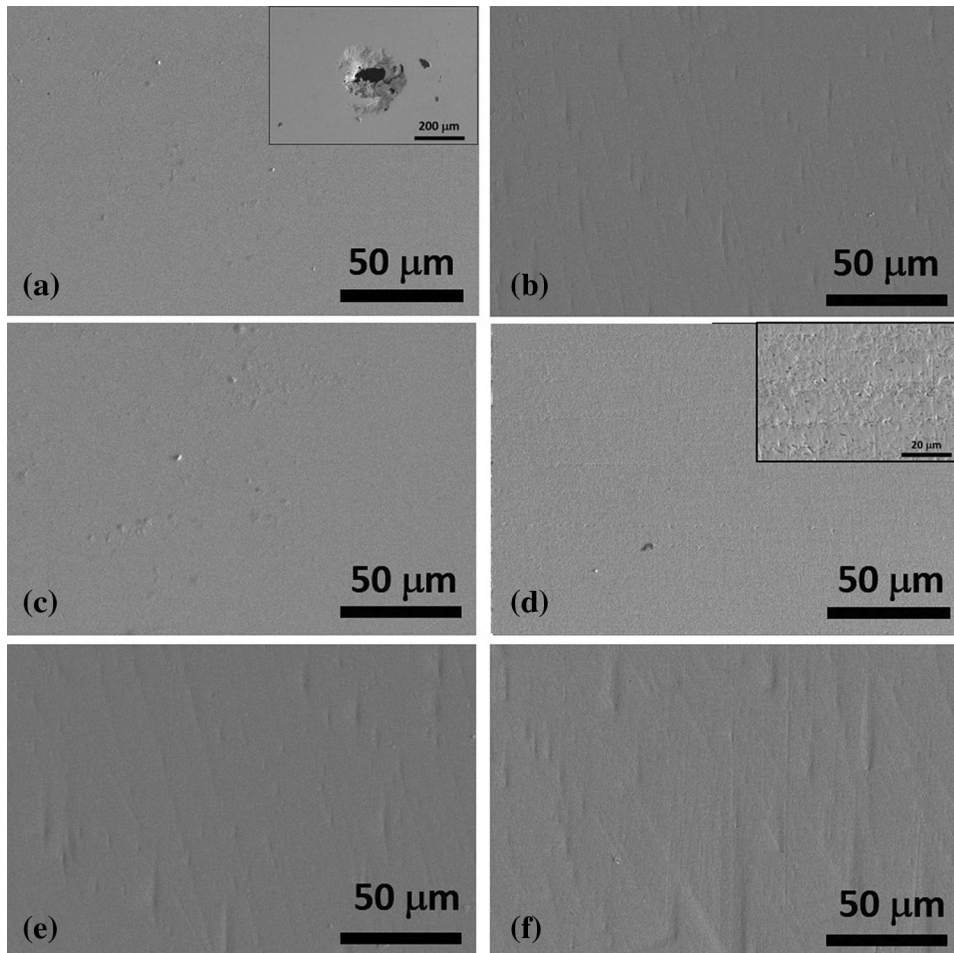


**Fig. 5** SEM micrographs showing the surface condition after dynamic polarization test in Hank's simulated body fluid (a) as-received, (b) cold-rolled, (c) annealed at 400 °C, (d) annealed at 600 °C (e) annealed at 800 °C and (f) annealed at 1000 °C

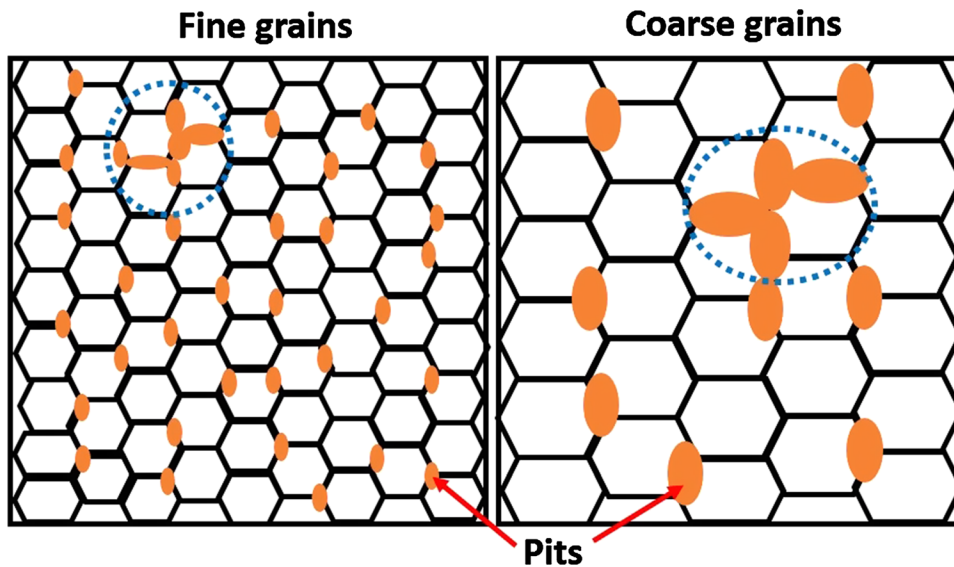


**Fig. 6** Schematic showing the mechanism of corrosion in fine and coarse grained samples

further increased to  $340 \pm 11$  after annealing at 400 °C. This could be due to the precipitation of HCP  $\alpha$ -phase at 400 °C as discussed earlier and also reported elsewhere (Ref 20).

However, reduction in micro-hardness after annealing at relatively higher temperature has been observed which could

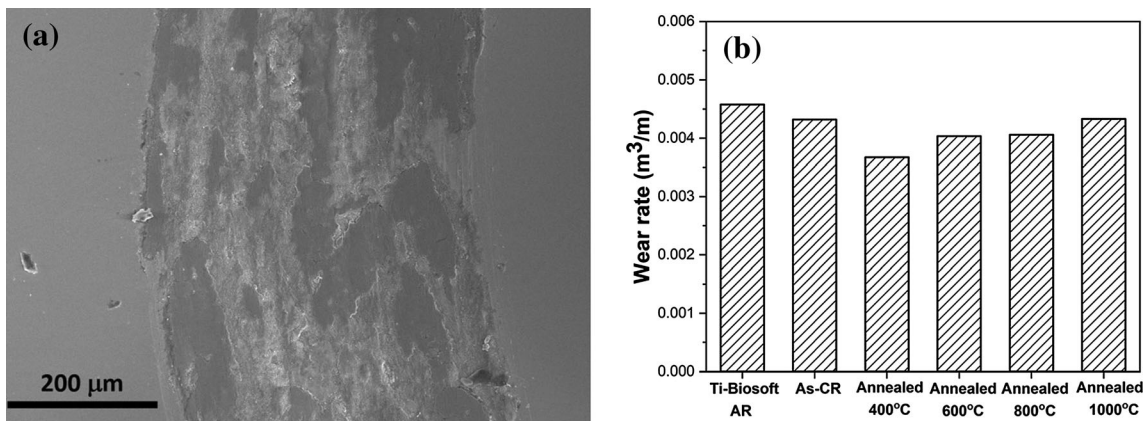


**Fig. 7** (a) SEM micrograph of worn-out as-received sample showing wear track (b) variation of wear rate

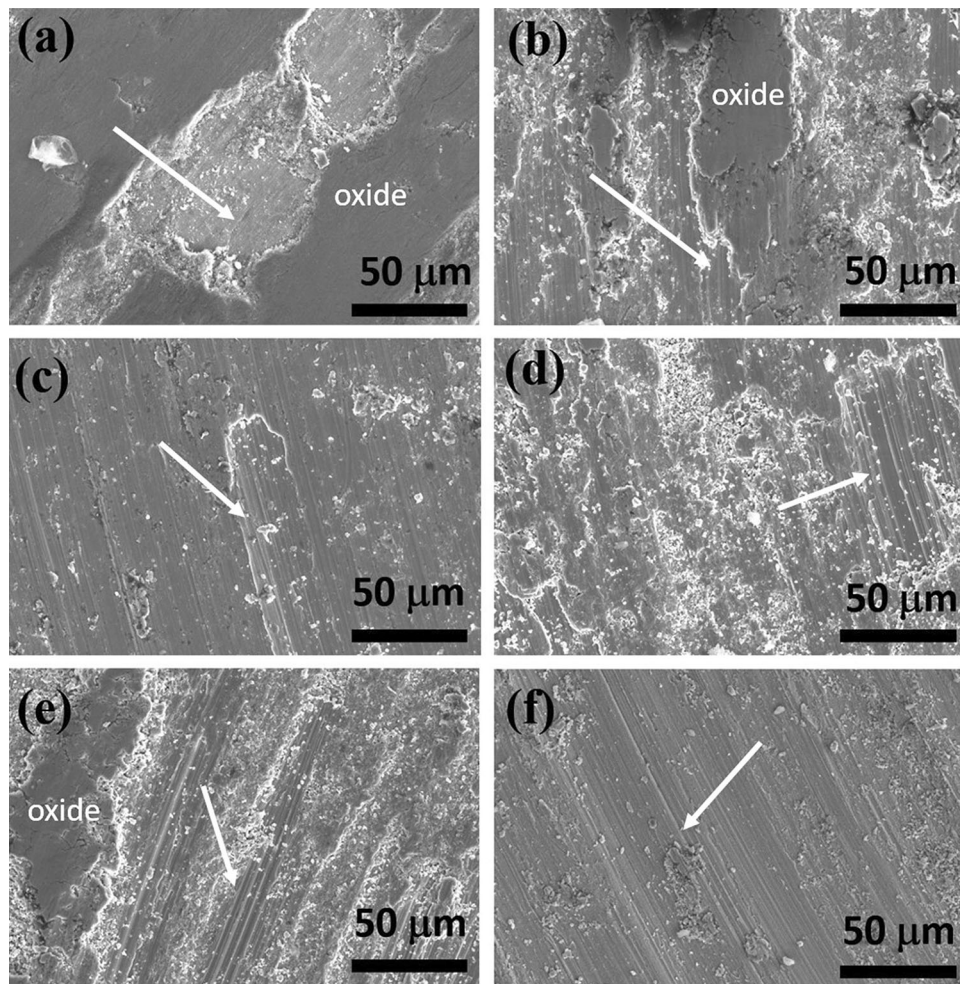


**Fig. 8** SEM micrographs showing the surface condition after wear test of (a) as-received, (b) cold-rolled, (c) annealed at 400 °C, (d) annealed at 600 °C (e) annealed at 800 °C and (f) annealed at 1000 °C

be due to the combined effect of decrease in the fraction of HCP  $\alpha$ -phase and recrystallization.

Effect of cold rolling and subsequent annealing at various temperatures on sliding wear behavior of the Ti-25Nb-25Zr alloys has been analyzed. Wear rate ( $W$ ) has been estimated by the ratio of wear volume to sliding distance. Wear volume has been determined using Eq 1 (Ref 29)

$$\text{wear volume } (v) = h \cdot A_n \quad (\text{Eq 1})$$

where,  $h$  is depth of wear and  $A_n$  is area. The depth of wear ( $h$ ) is taken as maximum depth of wear as obtained from the tribometer, whereas area  $A_n$  is determined from the SEM micrographs of wear track as shown in Fig. 7(a) as a

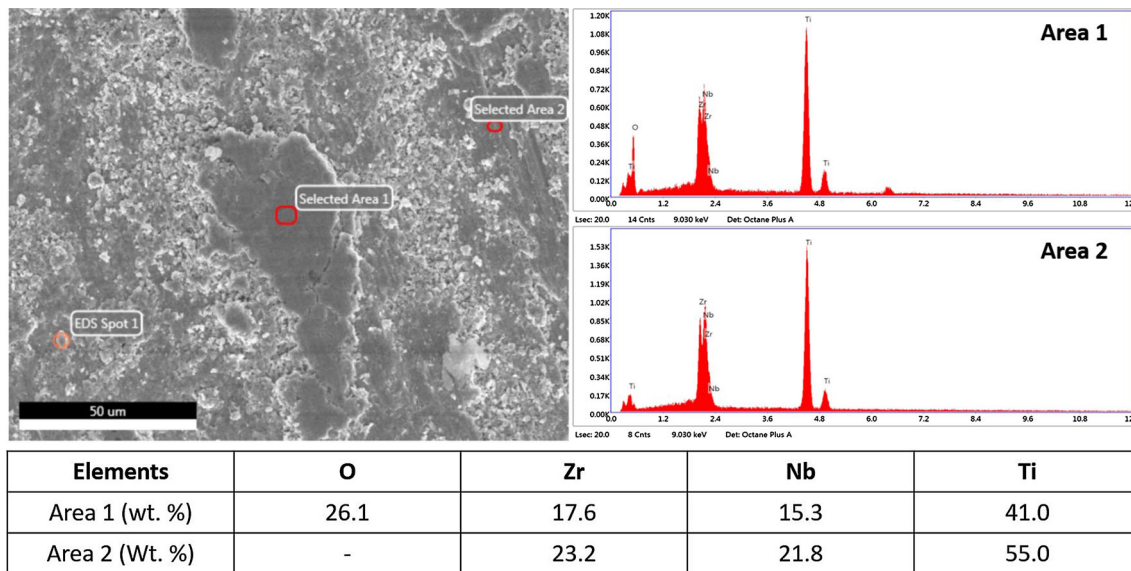


**Fig. 9** EDS analysis of worn out surface showing oxide formation

representative image. The variation of wear rate with different processing conditions is shown in Fig. 7(b). It is clear that wear rate of the cold rolled sample is lower than that of the as-received sample. Further decrease in wear rate can be noticed in Fig. 7(b) after annealing at 400 °C. Wear rate increases after annealing at temperatures greater than 600 °C. Wear rate is inversely proportional to the hardness of the material as suggested by Archards' equation (2) (Ref 21)

$$W = K \frac{P}{H} \quad (\text{Eq 2})$$

where,  $W$  is wear rate,  $P$  is applied pressure,  $H$  is hardness of the material and  $K$  is a dimensionless constant known as wear coefficient. Therefore, the variation in wear rate could be due to hardness variation in the sample. The Sample annealed at 400 °C has exhibited minimum wear rate (or maximum wear resistance), which can be attributed to its highest hardness among all the samples.

In order to understand the mechanism of wear, worn-out surfaces have been examined using SEM and corresponding micrographs are shown in Fig. 8(a-f). Scratch marks as shown with the arrow-heads can be noticed in all the micrographs, which could have formed due to the abrading action of debris produced during wear. It suggests that abrasive wear could be the governing wear mechanism. Zheng et al. (Ref 30) have also reported the abrasive wear as a governing mechanism in Ti-Zr-Nb-Ta alloys at low loads. It can also be noticed that scratch marks are relatively deeper in case of samples annealed at temperature greater than 600 °C (Fig. 8a-f) resulting in increased wear rate. This could be due to the relatively lower hardness of the samples annealed at higher temperature as compared to that of the cold rolled and sample annealed at 400 °C. Some dark gray layer can be noticed in the micrographs marked as oxide layer (Fig. 8a-f). Oxide layer has been confirmed by EDS analysis of the worn-out surfaces as shown in Fig. 9. EDS analysis reveals the significantly higher oxygen content in dark gray region (Area 1) as compared to that in Area 2. During sliding wear in air, the tribo-oxidation occurs due to local increase in temperature. Oxide layer forms and gets

removed in the subsequent engagement with the counter-body and fresh surface comes in contact in subsequent cycles.

Therefore, it is clear that corrosion and wear behavior of the Ti-25Nb-25Zr alloy has been affected by the cold rolling and subsequent annealing. The corrosion resistance has been found to improve by introducing crystallographic texture via cold-rolling and increase in grain size. On the other hand, wear resistance of the sample annealed at 400 °C has been found to be highest due to its highest hardness among all the samples.

## 4. Conclusions

In present work, the samples of the Ti-25Nb-25Zr alloy have been cold-rolled and annealed at 400, 600, 800 and 1000 °C. Annealing at different temperature has caused stress-relieving as well as recrystallization and grain growth resulting in different grain sizes. It has been found that the sample annealed at 400 °C has highest corrosion resistance in Hank's simulated body fluid solution. Improvement in corrosion resistance with increase in grain size of Ti-25Nb-25Zr alloys has also been found. Cold rolling and subsequent annealing have resulted in an improvement in passivation behavior. The sample of the Ti-25Nb-25Zr alloy annealed at temperature 400 °C has exhibited highest wear resistance due to its higher hardness. Abrasive wear has been observed to be the dominating wear mechanism.

## References

1. M. Peters, J. Kumpfert, C.H. Ward and C. Leyens, Titanium alloys for Aerospace Applications, *Adv. Eng. Mater.*, 2003, **5**, p 419-427
2. M. Niinomi, Recent Research and Development in Metallic Materials for Biomedical, Dental and Healthcare Products Applications, *Mater. Sci. Forum.*, 2007, **539-543**, p 193-200
3. S. Bahl, S. Suwas and K. Chatterjee, Comprehensive Review on Alloy Design, Processing, and Performance of  $\beta$  Titanium alloys as Biomedical Materials, *Inter. Mater. Rev.*, 2020 <https://doi.org/10.1080/09506608.2020.1735829>



4. I. Mutlu, S. Yenyol and E. Oktay, Characterisation of Corrosion Properties of Ti-Nb-Cu alloy Foam by Electrochemical Impedance Spectroscopy Method, *Corros. Eng. Sci. Technol.*, 2016, **51**, p 110-117
5. S. Nag, R. Banerjee and H.L. Fraser, Microstructural Evolution and Strengthening Mechanisms in Ti-Nb-Zr-Ta, Ti-Mo-Zr-Fe and Ti-15Mo Biocompatible Alloys, *Mater. Sci. Eng. C*, 2005, **25**, p 357-362
6. P.R. Walker, J. LeBlanc and M. Sikorska, Effects of Aluminum and other Cations on the Structure of Brain and Liver Chromatin, *Biochemistry*, 1989, **28**, p 3911-3915
7. W.F. Ho, C.P. Ju and J.H. Lin, Structure and Properties of Cast Binary Ti-Mo alloys, *Biomaterials*, 1999, **20**, p 2115-2122
8. Y. Song, D.S. Xu, R. Yang, D. Li, W.T. Wu and Z.X. Guo, Theoretical study of the Effects of Alloying Elements on the Strength and Modulus of  $\beta$ -type Bio-titanium alloys, *Mater. Sci. Eng. A*, 1999, **260**, p 269-274
9. M. Geetha, A.K. Singh, R. Asokamani and A.K. Gogia, Ti Based Biomaterials, The Ultimate Choice For Orthopaedic Implants - A Review, *Prog. Mater. Sci.*, 2009, **54**, p 397-425
10. L.S. Kubie and G.M. Shults, Studies on the Relationship of the Chemical Constituents of Blood and Cerebrospinal Fluid, *J. Exp. Med.*, 1925, **42**, p 565-591
11. H. Emnéus and U. Stenram, Metal implants in the human body: A histopathological study, *Acta. Orthop. Scandinav.*, 1965, **36**, p 115-126
12. G. Manivasagam, D. Dhinasekaran and A. Rajamanickam, Biomedical Implants: Corrosion and its Prevention—A Review, *Recent Patents Corros. Sci.*, 2010, **2**, p 40-54
13. Y.H. Jeong, H.C. Choe and S.W. Eun, Hydroxyapatite Coating on the Ti-35Nb-xZr Alloy by Electron Beam-Physical Vapor Deposition, *Thin Solid Films*, 2011, **519**, p 7050-7056
14. M. Geetha, U.K. Mudali, A.K. Gogia, R. Asokamani and B. Raj, Influence of Microstructure and Alloying Elements on Corrosion Behavior of Ti-13Nb-13Zr alloy, *Corros. Sci.*, 2004, **46**, p 877-892
15. C. Kuphasuk, Y. Oshida, C.J. Andres, S.T. Hovijitra, M.T. Barco and D.T. Brown, Electrochemical Corrosion of Titanium and Titanium-based Alloys, *J. Prosthet. Dent.*, 2001, **85**, p 195-202
16. M.A. Khan, R.L. Williams and D.F. Williams, In-vitro Corrosion and Wear of Titanium Alloys in the Biological Environment, *Biomaterials*, 1996, **17**, p 2117-2126
17. P.A. Dearnley, A Brief Review of Test Methodologies for Surface-engineered Biomedical Implant Alloys, *Surf. Coat. Technol.*, 2005, **198**, p 483-490
18. R. Sahoo, S. Mantry, T.K. Sahoo, S. Mishra and B.B. Jha, Effect of Microstructural Variation on Erosion Wear Behavior of Ti-6Al-4V alloy, *Tribol. Trans.*, 2013, **56**, p 555-560
19. S.J. Li, R. Yang, S. Li, Y.L. Hao, Y.Y. Cui, M. Ninomi and Z.X. Guo, Wear characteristics of Ti-Nb-Ta-Zr and Ti-6Al-4V alloys for Biomedical Applications, *Wear*, 2004, **257**, p 869-876
20. K.D. Ralston and N. Birbilis, Effect of Grain Size on Corrosion: A Review, *Corrosion*, 2010, **66**, p 075005-075005-13
21. A. Balyanov, J. Kutnyakova, N.A. Amirkhanova, V.V. Stolyarov, R.Z. Valiev, X.Z. Liao, Y.H. Zhao, Y.B. Jiang, H.F. Xu, T.C. Lowe and Y.T. Zhu, Corrosion Resistance of Ultra fine-grained Ti, *Scr. Mater.*, 2004, **51**, p 225-229
22. M. Hoseini, A. Shahryari, S. Omanovic and J.A. Szpunar, Comparative Effect of Grain Size and Texture on the Corrosion Behaviour of Commercially Pure Titanium Processed by Equal Channel Angular Pressing, *Corros. Sci.*, 2009, **51**, p 3064-3067
23. S.K. Vajpai, B. Sharma, M. Ota and K. Ameyama, Effect of Cold Rolling and Heat-Treatment on the Microstructure and Mechanical Properties of  $\beta$ -Titanium Ti-25Nb-25Zr alloy, *Mater. Sci. Eng. A*, 2018, **736**, p 323-328
24. P.K. Rai, S. Shekhar and K. Mondal, Effects of Grain Size Gradients on the Fretting Wear of a Specially-Processed Low Carbon Steel against AISI E52100 Bearing Steel, *Wear*, 2018, **412-413**, p 1-13
25. P.K. Rai, S. Shekhar, K. Yagi, K. Ameyama and K. Mondal, Corrosion Behavior of Harmonic Structured 316L Stainless Steel in 3.5% NaCl and Simulated Body Fluid Solution, *J. Mater. Eng. Perform.*, 2019, **28**, p 7554-7564
26. ASTM Standard G 102-89, Standard practice for calculation of corrosion rate and related information from electrochemical measurements, ASTM International, West Conshohocken, PA (2014)
27. J. Zhang, F. Sun, Y. Hao, N. Gozdecki, E. Lebrun, P. Vermaut, R. Portier, T. Gloriant, P. Laheurte and F. Prima, Effect of equiatomic Zr/Nb substitution on super elastic behavior of Ti-Nb-Zr alloy, *Mater. Sci. Eng. A*, 2013, **563**, p 78-85
28. K. Guo, T. Wang, K. Meng, C. Yao and Q. Wang, Influence of Cold Rolling Deformation on Mechanical Properties and Corrosion Behavior of Ti-6Al-3Nb-2Zr-1Mo alloy, *Mater. Res. Express.*, 2020, **7**, p 066511
29. G. Straffelini, *Friction and Wear*, Springer, AG Switzerland, 2015
30. Z. Zheng, Z. Wang and W. Huang, Influence of Load and Sliding Distance on the Micro-scale Abrasive Wear Behavior of TZNT alloy, *J. Chinese Adv. Mater. Soc.*, 2016, **4**, p 82-90

**Publisher's Note** Springer Nature remains neutral with regard to jurisdictional claims in published maps and institutional affiliations.